Synthesis of Hexagonal $BaTa_2O_6$ Nanorods and Influence of Defects on the Photocatalytic Activity

Tongguang Xu, Xu Zhao, and Yongfa Zhu*

Department of Chemistry, Tsinghua University, Beijing, 100084, China

Received: August 16, 2006; In Final Form: September 29, 2006

Hexagonal barium tantalate ($BaTa_2O_6$) nanorods were synthesized by a hydrothermal method based on the reaction of concentrated $Ba(OH)_2$ solution and Ta_2O_5. $BaTa_2O_6$ samples show a uniform cylindrical structure with diameters of 5−30 nm and the lengths of 50−200 nm. The formation of $BaTa_2O_6$ nanorods follows a dissolution−recrystallization mechanism and is governed by hydrothermal temperature and time. $BaTa_2O_6$ nanorod samples prepared at 270 °C for 72 h have exhibited the highest photocatalytic activity in the degradation of Rhodamine B (RhB) in aqueous solution under UV radiation. Hydrogen-related defects were detected in $BaTa_2O_6$ nanorods, which originate from the oxygen octahedron. The number of defects was dependent on the hydrothermal temperature, and the photocatalytic activities of $BaTa_2O_6$ nanorods increase with the decrease of defect amounts. On the basis of the experiment results, the difference in photocatalytic activities for samples is mainly caused by lattice defects, which can act as inactivation centers.

1. Introduction

Semiconductor photocatalysts have attracted much attention due to their potential applications in splitting of water, degradation of toxic substances, and solar cells.[1−3]Among various semiconductor photocatalysts, TiO_2 has been widely researched due to its chemical stability, nontoxicity, and high photocatalytic reactivity under ultraviolet (UV) irradiation.[3]Although much work has been devoted to the improvement of photocatalytic performance of TiO_2, the improvement of activity is limited.[4−6] Therefore, it is very important to develop a new type of photocatalyst with high photocatalytic activity. In recent years, varieties of metal complex oxides such as titanates, niobates, and tantalates have also been found to exhibit photocatalytic activity. As for some photocatalysts, cocatalysts and additives are indispensable for water splitting.[7] However, tantalates have exhibited high photocatalytic activities for water splitting even in the absence of a cocatalyst.[8−10] These tantalates consist of corner-shared TaO_6 octahedra in their crystal structures, and the bond angle of Ta−O−Ta is close to 180°.[7,9c] Thus, the photogenerated electron−hole pairs can migrate easily in the corner-shared framework of TaO_6 units, which is beneficial to the photocatalysis reaction.

In general, these tantalate photocatalysts are mainly synthesized via the conventional solid-state reaction (SSR) route or melt growth at high temperatures (typically 1000−1300 °C).[7−10] The common problems in the SSR route are the growth of crystal, segregation of components, and possible loss of stoichiometry due to volatilization of the constituent components at high temperatures. These factors result in the decrease of photocatalytic activity. Recently, low-temperature, wet-chemical routes have been employed to prepare nanosized crystallites with higher purity and uniform sizes to enhance photocatalytic activity.[11−14] It has been found that the reaction between fine metal oxide powder or a precipitate of a transition metal hydrate and concentrated alkaline solution under moderate hydrothermal conditions is an effective approach to achieve one-dimensional (1D) structures of metal oxides and hydroxides with nanometer-scale dimensions.[15−18] These 1D-nanostructure materials have exhibited novel reaction behaviors and unique physicochemical properties.[19] Thus, it is very interesting and significant to prepare tantalate photocatalysts with 1D structures, investigate their formation mechanism, and explore their photocatalytic activities.

$BaTa_2O_6$ is an excellent ferroelectric material with a tungsten−bronze type structure. It has three polymorphs: orthorhombic phase, tetragonal phase, and hexagonal phase. Kudo et al. exhibited that $BaTa_2O_6$ has certain photocatalytic activities toward water splitting, and the orthorhombic phase shows much higher photocatalytic activity over the other forms.[9b] $BaTa_2O_6$ is a wide-gap semiconductor with a gap of 3.94 eV and can be used as a photocatalyst under UV irradiation. In $BaTa_2O_6$, the valance band originates from fully filled O^{2p} bonding orbitals, and the conduction band comes from Ta5d nonbonding orbitals (t^{2g}) in TaO_6 octahedra. The network, chains, or slabs which are formed by corner-shared octahedral units of TaO_6 may increase the mobility of the charged particles in the crystal.[7,10] This will promote the immigration of photoinduced electrons and holes and result in high photocatalytic activity. However, in $BaTa_2O_6$, TaO_6 units form edge-sharing pairs (Ta_2O_{10}) and are connected with each other by corner-sharing to form layer networks.[10] The photocatalytic activity of $BaTa_2O_6$ synthesized via the SSR method is low, and its photophysical and photochemical properties are little known. The objective of this research is to develop a method to control the microstructural, crystal phase of 1D $BaTa_2O_6$, explore its photocatalytic activities in degrading organic contaminants, and explore the relationship between nanorod structure and photocatalytic activity. Herein, a one-step, template-free, seedless method to prepare $BaTa_2O_6$ nanorods directly from tantalum oxide under hydrothermal conditions has been reported for the first time. The nanostructure of $BaTa_2O_6$ nanorods can be easily controlled by adjusting the hydrothermal temperature and time. The formation mechanism has been investigated in detail. $BaTa_2O_6$ nanorod photocatalysts show high photocatalytic activity toward degrad-

* Corresponding author. E-mail: zhuyf@tsinghua.edu.cn; Fax: +86-10-62787601; Tel:+86-10-62787601.

10.1021/jp065307k CCC: $33.50
Published on Web 12/02/2006

ing Rhodamine B (RhB) under UV irradiation. On the basis of our work, it is found that the defects in $BaTa_2O_6$ crystals predominantly affect the photocatalytic activity.

2. Experimental Section

2.1. Preparation of $BaTa_2O_6$ Nanorods. Hydrothermal treatment was applied to synthesize $BaTa_2O_6$ nanorods. All reagents were of analytical grade without further purification. In a typical experiment, 0.630 g of $Ba(OH)_2 \cdot 8H_2O$ was dissolved in water (60 mL), to which 0.884 g of Ta_2O_5 powder was then added under stirring, meaning that the mole ratio of was 1:1. After 10 min of stirring, the solution was transferred into a Teflon-lined stainless steel autoclave of 100 mL capacity and then sealed. The autoclave was maintained at 270 °C for 48 h and cooled naturally to room temperature. The sample formed at the bottom of the autoclave was centrifuged, filtered out, and washed with deionized water to pH 7. Finally, the sample was dried at 60 °C for 1 h in air. To investigate the reaction mechanism, the same reaction was carried out, and the reaction mixture was taken at regular intervals of 24 h.

2.2. Characterization. X-ray diffraction measurements were carried out with a Bruker D 8 Advance Powder X-ray diffractometer with a Cu Kα (λ = 1.5418 nm) radiation source. Diffraction patterns were collected from 10° to 70° at a speed of 4°/min. The average crystalline size of samples was calculated by using the Scherrer formula, taking the full-width at half-maximum (fwhm) of the diffraction peak. Raman spectra were acquired with a Raman microspectrometer (Renishaw 1000 NR) using an Ar ion laser (632.8 nm). Raman spectra were measured under a microscope using a 20× objective to focus the incident excitation laser radiation into a spot of 1−2 mm or 2−3 mm diameter, respectively, and to collect the scattered light. The laser power was kept low enough to avoid heating of the samples by optical filtering and/or defocusing of the laser beam at the sample surface. Spectra were collected in the range of 1000−200 cm^{-1} with a resolution of 1 cm^{-1}. Photoluminescence (PL) spectra of $BaTa_2O_6$ nanorods were measured with a Perkin-Elmer 4500 fluorescence spectrophotometer. Each sample was dry-pressed into a 10-mm-diameter round disk containing about 200 mg of mass. The sample disks were illuminated with an excitation wavelength of 280 nm at room temperature. The diffuse reflectance UV−vis absorption spectra were collected on a UV−vis spectrometer (UV3010, Hitachi). $BaSO_4$ was used as the reflectance standard in the experiment. Infrared transmission spectra were recorded for KBr disks containing the powdered sample with an FTIR spectrometer (Perkin-Elmer 1600). The size, morphology, and chemical composition of the as-prepared $BaTa_2O_6$ nanorod samples were analyzed by TEM. Low-magnification TEM was carried out on a JEOL-JEM 100 microscope, working at an 120 kV accelerating voltage. HRTEM images and SAED patterns as well as EDS data were obtained on a JEOL 2010 HRTEM (equipped with an Oxford INCA EDS system) at an accelerating voltage of 200 kV. Specimens for these tests were prepared by ultrasonically dispersing the products into absolute ethanol and then depositing an aqueous drop of these samples onto a 300 mesh Cu grid, coated with a carbon film. BET surface areas of the samples were determined by nitrogen adsorption−desorption isotherm measurement at 77 K (Micromeritics Automatic Surface Area Analyzer Gemini 2360, Shimadzu).

2.3. Evaluation of Photocatalytic Activity. The photocatalytic activity of $BaTa_2O_6$ samples was tested for the degradation of Rhodamine-B in aqueous solution. An 11-W bactericidal lamp with 254 nm was used as the light source. In each run, 0.10 g of $BaTa_2O_6$ catalyst was added into 200 mL of RhB solution (2×10^{-5} mol·L^{-1}). Prior to photocatalytic reaction, the suspension was magnetically stirred in the dark, and the concentration of RhB was monitored. The concentration of RhB did not change after stirring for 30 min, which indicates that it is enough to reach the adsorption equilibrium of RhB for 30 min. Therefore, all of the suspensions were stirred for 30 min in the dark to ensure adsorption equilibrium before illumination. The solution concentration was about 30 mg/L, and the pH value of the solution was nearly 7.5. The suspension samples including the photocatalyst and RhB were separated by the centrifuge, and the solution samples were analyzed by UV−visible (Hitachi UV−vis 3010) spectrometer.

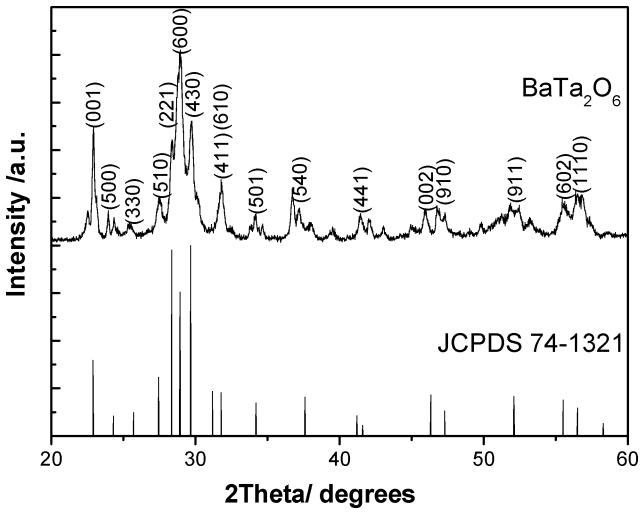

Figure 1. XRD patterns of the $BaTa_2O_6$ nanorod sample obtained by hydrothermal reaction of Ta_2O_5 particles and $Ba(OH)_2$ solution.

Photoelectrochemical measurements were carried out in a 100-mL glass reactor under UV illumination. An 11-W bacterial lamp was used as UV light source. For photocurrent measurements, 25 mg of photocatalyst was suspended in distilled water (75 mL) containing acetate (1 M) and Fe^{3+} (1 mM) as an electron donor and acceptor, respectively, and the pH value of suspension was adjusted to 1.95 ± 0.05 with $HClO_4$. A platinum plate (1 × 1 cm^2, 0.125 mm thick, both sides exposed to the solution), a saturated calomel electrode (SCE), and a platinum gauze were immersed in the reactor as a working collector, reference, and counter electrode, respectively. Photocurrents in the suspension were measured by applying a potential (+0.6 V vs SCE) to the Pt working electrode using a potentiostat (CHI-660B).

3. Results and Discussion

3.1. Structure and Morphology of $BaTa_2O_6$ Nanorods. The crystal structure of $BaTa_2O_6$ nanorod sample was revealed by X-ray diffraction (XRD). Figure 1 shows XRD patterns of $BaTa_2O_6$ nanorod samples. All peaks correspond to hexagonal phase of $BaTa_2O_6$, which is in agreement with the literature (JCPDS No. 74-1321). $BaTa_2O_6$ has three polymorphs such as orthorhombic with a $CaTa_2O_6$-type structure, tetragonal with a tetragonal tungsten−bronze structure, and hexagonal with a hexagonal tungsten bronze-related structure.[20] Only $BaTa_2O_6$ with a hexagonal phase can be obtained under the present hydrothermal conditions. It is very interesting that the peak of (600) is the strongest for $BaTa_2O_6$ nanorods while the (430) peak is the strongest in the solid-state-reaction $BaTa_2O_6$. The intensity ratio of the (600) peak with the (430) peak is 1.5 for $BaTa_2O_6$ nanorods, while it is 0.75 in the standard card. The

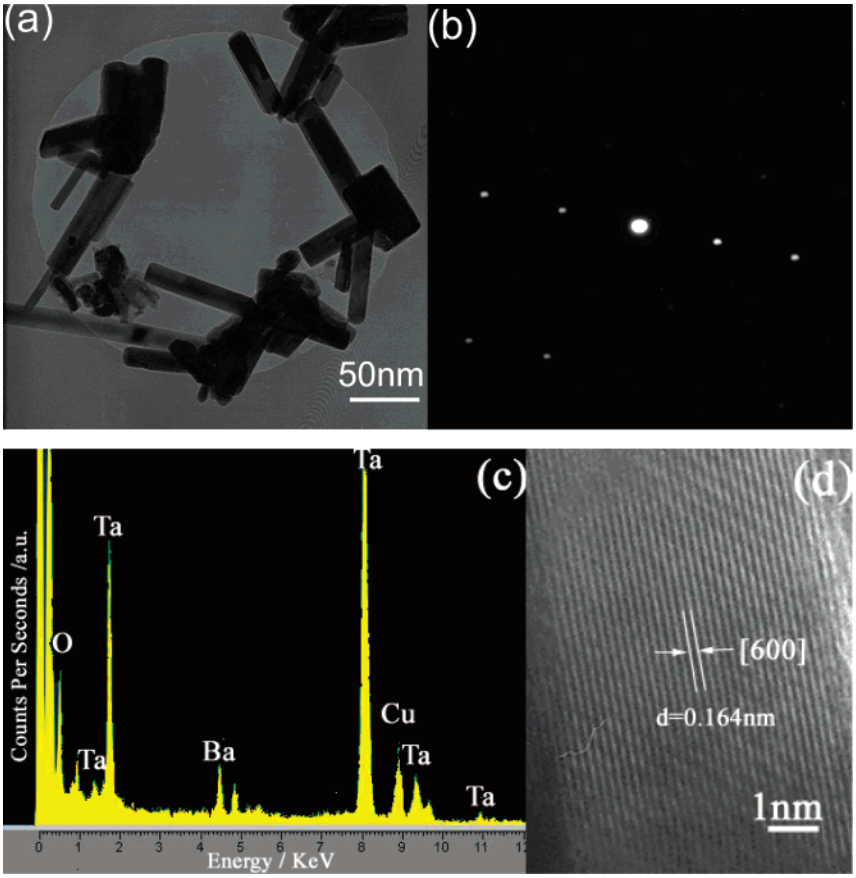

Figure 2. (a) TEM image of the $BaTa_2O_6$ nanorod sample. (b) SAED pattern of a $BaTa_2O_6$ nanorod. (c) Energy dispersive X-ray spectrum of $BaTa_2O_6$ showing Ba, Ta, and O peaks; C and Cu peaks are due to TEM grid. (d) HRTEM image of the tip of a $BaTa_2O_6$ nanorod showing clear lattice fringes.

increase of intensity ratio of the (600) peak with the (430) peak suggests that the $BaTa_2O_6$ nanorods grow in the (600) direction. The peaks of $BaTa_2O_6$ sample hydrothermally synthesized are wider than that of the SSR sample, indicating that hydrothermal samples are nanocrystallite.

The morphology and lattice structure of $BaTa_2O_6$ nanorods were further examined by TEM. The TEM image of $BaTa_2O_6$ nanorod prepared at 270 °C is shown in Figure 2a. $BaTa_2O_6$ sample shows a uniform cylindrical structure with diameter of 5−30 nm and length of 50−200 nm. SAED pattern shows the sharp diffraction spots, indicating the $BaTa_2O_6$ nanorod with crystalline structure (Figure 2b). The compositions of the nanorod are determined by EDS (Figure 2c). The result reveals that the $BaTa_2O_6$ nanorod sample is composed of barium, tantalum, and oxygen, as expected with a near stoichiometric ratio Ba:Ta:O = 1:2:5.8. The evidence for the formation of single-crystalline $BaTa_2O_6$ nanorods could be found in the high-resolution TEM (HR-TEM) image as shown in Figure 2d.There are no observable domain boundaries, and lattice fringes run continuously toward the interior of the nanorod, which can be more clearly seen. This further confirms the crystalline nature of these nanorods. On the basis of the calculation of the lattice spacing and the analysis of its orientation, it is found that the nanorod grows preferentially along the [600] direction.

Figure 3 shows XRD patterns for the samples prepared at various hydrothermal temperatures for 48 h. The hydrothermal temperature takes an important role during the formation of $BaTa_2O_6$ nanorods. After hydrothermal reaction at 220 °C for 48 h, the XRD pattern of the sample remains the same as that of Ta_2O_5, implying that $BaTa_2O_6$ did not form. With the increase

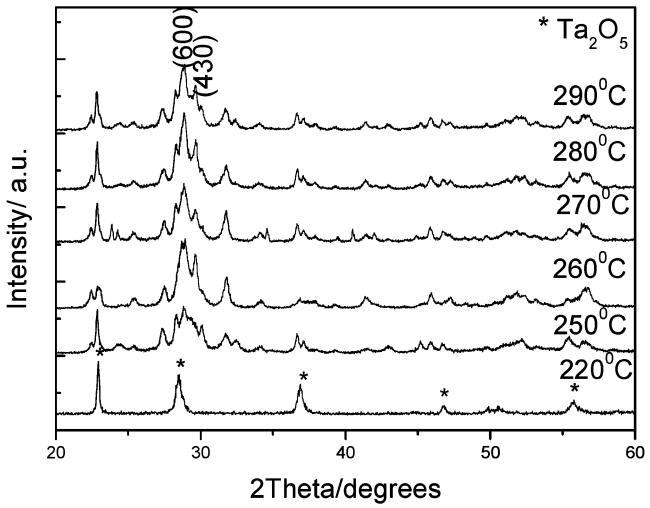

Figure 3. XRD patterns of nanorod samples synthesized by reaction of Ta_2O_5 and $Ba(OH)_2$ at various temperatures for 48 h.

of hydrothermal temperature, the relative intensity of the peaks which were attributed to the Ta_2O_5 phase decrease gradually, some new peaks form, and a coexistent phase appears and strengthens. The XRD patterns of sample obtained at 250 °C are profoundly different from that of Ta_2O_5, suggesting that the reaction between $Ba(OH)_2$ and Ta_2O_5 takes place substantially. As the temperature is raised to 270 °C, $BaTa_2O_6$ with hexagonal structure is formed completely. It can also be found that the intensity of the (600) peak becomes higher than that of (430), which is different from the literature.[20] Phase transitions from

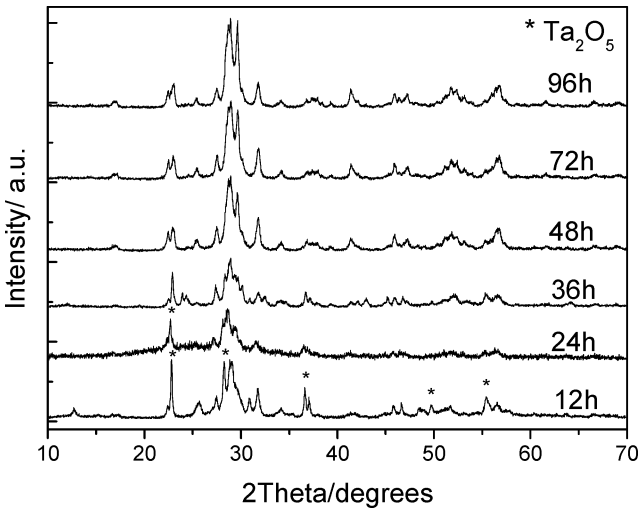

Figure 4. XRD patterns of nanorods synthesized by reaction at 270 °C for different reaction times.

hexagonal to other phases are not observed as the reaction temperature rises to 290 °C. Hence, the reaction temperature is an important factor to govern the formation of $BaTa_2O_6$ crystals, and the optimal temperature for the formation of barium tantalate by hydrothermal method is above 270 °C.

XRD patterns of the sample reacted at 270 °C for various times are shown in Figure 4. XRD patterns of the samples obtained at 270 °C for 12 and 24 h are distinctly different from that of Ta_2O_5. The diffraction peaks of the raw sample (Ta_2O_5) are still observed in samples (12 h, 24 h), suggesting that the sample contains more than one phase and the hydrothermal reaction is not completed. When the reaction time is maintained at 36 h, some peaks of $BaTa_2O_6$ phase appear, but the crystallinity is poor. After the reaction time reaches 48 h, a well-crystallized $BaTa_2O_6$ nanorod phase with regular shape was formed from the poorly crystallized samples in the subsequent period. The intensity of the diffraction peak becomes stronger as the reaction time lengthens. It can be concluded that the reaction time is an important factor for the hydrothermal synthesis of $BaTa_2O_6$ nanorods under a lower concentration of alkali ($[OH^-] = 0.06$ mol/L).

3.2. Formation Mechanism of $BaTa_2O_6$ Nanorods. A comprehensive formation mechanism of tantalate nanorods is not yet available. The morphology of samples prepared at 270 °C for various reaction times were measured by TEM in order to understand the formation processes of the tantalate nanorods. In the early stages (270 °C for 24 h), both nanorods and aggregated nanoparticles are found (Figure 5a). It also can be observed that the short nanorods grow on the surfaces of the aggregated nanoparticles (Ta_2O_5). As the reaction time is prolonged, the irregular nanoparticles vanished and longer nanorods formed (Figure 5b, 5c), suggesting that the nanorods grow longer at the consummation of the small particles due to the difference in solubility between the larger particles and the small particles according to Gibbs−Thomson law.[21] After prolonging the reaction time to 96 h at 270 °C, well-dispersed and elongated $BaTa_2O_6$ nanorods were obtained (Figure 5d). The formation mechanism of the anisotropic nanorod growth should be different from that of previous methods that depend on structure-directing templates.[22] We conclude that the growth of $BaTa_2O_6$ nanorods under the hydrothermal conditions is possibly subjected to the dissolution−crystallization mechanism. Under normal hydrothermal conditions, a highly supersaturated solution was adopted and amorphous fine particles acted as the precursors for the synthesis of nanocrystallines.[23] At the beginning, for the absence of a stabilizing agent, Ta_2O_5 particles partly dissolved and hydroxylated into the corresponding hydroxide,[24] i.e., $Ta_2O_5 \cdot xH_2O$ or $Ta(OH)_5$ under high temperature and high pressure, forming a variety of hydroxylated Ta−O ionic groups ($Ta_2O_6^{2-}$). The dissolved $Ta_2O_6^{2-}$ ions then react with Ba^{2+} ions in the reaction solution to form stable $BaTa_2O_6$ grains on the Ta_2O_5 hydroxide substrate by heterogeneous crystal growth. The formed $BaTa_2O_6$ nuclei may breakdown from the outer layer of the hydroxide, dissolve in the solution, and recrystallize into nanorods. This dissolution−recrystallization mechanism is repeated, forming successive nanorods of $BaTa_2O_6$. As time is lengthened, the longer nanorods grow at the cost of the shorter nanorods to reduce the surface energy. Interestingly, the diameter of $BaTa_2O_6$ nanorods is restricted to a narrow range and only changed slightly with temperature and time. It may be caused by the low chemical potential on the a and b axes. On the basis of the above results, it is reasonable to deduce that $BaTa_2O_6$ nanorod crystals originate from $BaTa_2O_6$ nanoparticles because the diameter of nanorods is near the same and these nanorods have grown in a preferential growth orientation. Thus, the length of $BaTa_2O_6$ nanorods is strongly correlated with reaction time and can be controlled via adjustment of the reaction time. This result implies that the aspect ratio of $BaTa_2O_6$ nanorods can be easily modulated with reaction time.

The promotion of anisotropic growth of nanorods in a ligand-free system is mainly governed by a general cooperative effect, including the intrinsic structure feature of specific faces, the local solution details, the foreign energy activation, and the autogenous pressure.[23] Peng et al. have shown that the shape of nanorods is strongly dependent on the relative chemical potential.[25a] According to Gibbs−Thomson theory, the relative chemical potential of crystals is simply proportional to their surface−atom ratio. It is believed that one-dimensional growth occurs only if the chemical potential of the monomers in the solution is much higher than the highest potential of the atoms on the surface of the nanocrystals.[25b] As for $BaTa_2O_6$, the (600) face perpendicular to the a-axis has the highest chemical potential compared with other facets. This structure feature makes the (600) faces very sensitive to the surrounding growth conditions. This intrinsic anisotropic growth could happen when enough outer energy input overcomes the reaction barrier. In addition, the closed-reaction environment under hydrothermal conditions will give a fast circulation rate of solute in solution, which could favor bringing the ions and anions into the right positions on the developing lattices faces more energetically.

3.3. Photocatalytic Activity and Relationship with Defects in $BaTa_2O_6$ Nanorods. Figure 6 shows the variation in absorption of RhB at 553 nm with the irradiation time. The blank test confirms that RhB was not degraded in the dark and only slightly degraded under UV light without catalysts, indicating that the photolysis and adsorption action of catalysts can be ignored. The maximum absorption of the degraded solution exhibited hypsochromic shifts with irradiation time, implying the cleavage of the conjugated structure of RhB and the decomposition of a series of N-deethylated intermediates.[26] As is shown in Figure 6, the degradation of RhB is found to follow pseudo-first-order kinetics. The sample prepared at 270 °C exhibits the highest photocatalytic activity ($k = 0.05494 \times 10^{-5}$ mol/L·min).

The immigration ability of electron in photocatalyst is critical factor to govern the photoefficiencies and can be directly evaluated by monitoring the photocurrent generation.[27] Figure

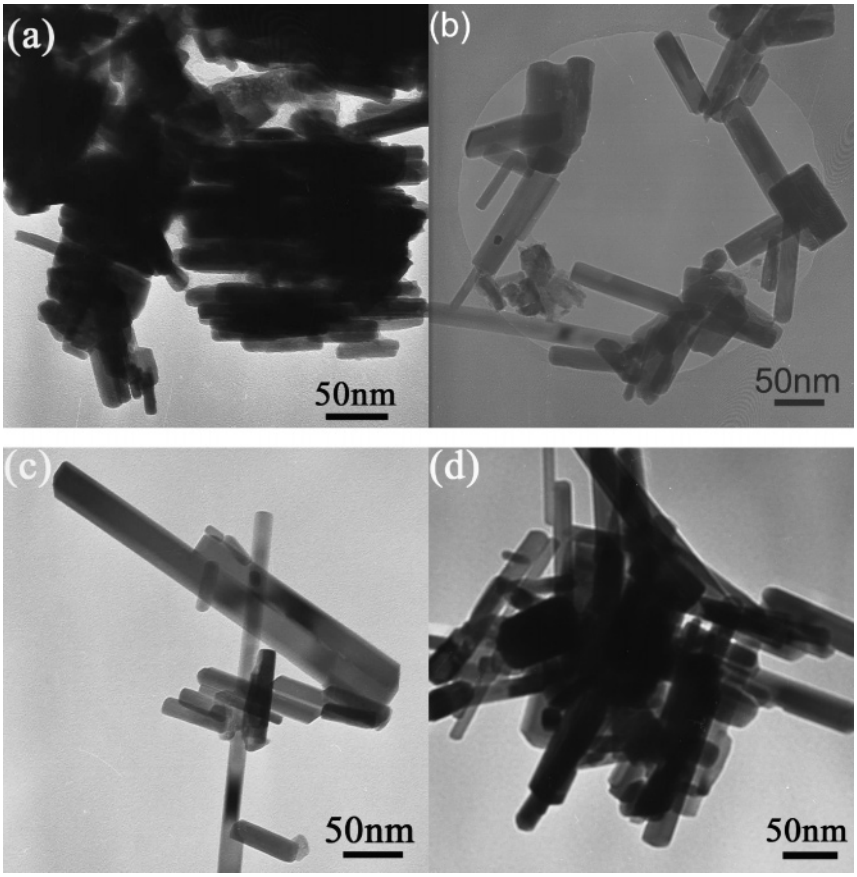

Figure 5. TEM images for the reaction intermediates taken from the hydrothermal reaction of $Ba(OH)_2$ and Ta_2O_5 after (a) 24 h, (b) 48 h, (c) 72 h, and (d) 96 h.

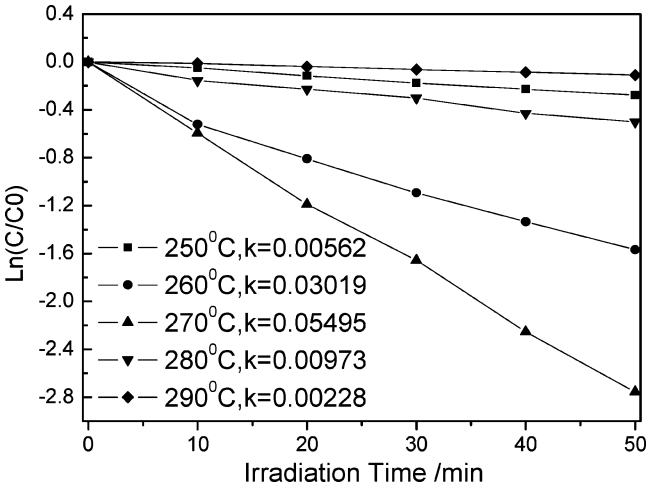

Figure 6. Photocatalytic decomposition curves of RhB by $BaTa_2O_6$ nanorod samples obtained at various temperatures for 48 h.

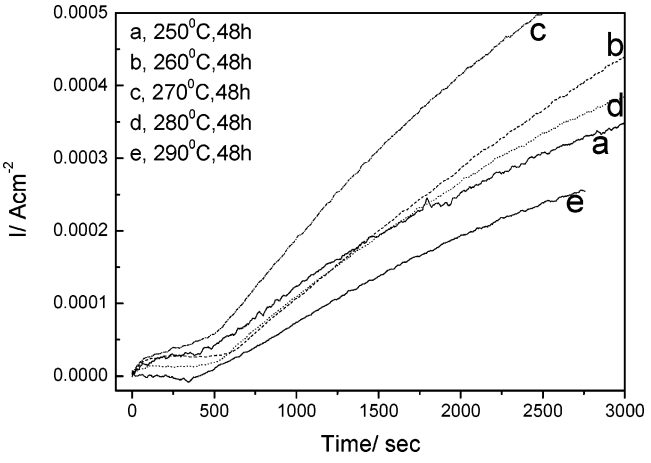

Figure 7. Photocurrent generated with UV irradiation on $BaTa_2O_6$ samples prepared at various temperatures for 48 h.

7 shows the photocurrents of photocatalysts generated in suspensions under UV light. $BaTa_2O_6$ nanorods obtained at 270 °C generate the highest photocurrent among all samples, while the photocurrent of the 290 °C sample is the lowest, which is only one-third of the 270 °C sample. It can also be found that the order of photocurrent values for the samples is consistent with the order of their photocatalytic activities, showing the photocurrent is positively relevant to the photocatalytic activity. The generation of photoelectrons is the critical initial step of photocatalytic reaction, and the rate directly governs the photocatalytic activity.

The photocatalytic activity of semiconductor oxides is mainly governed by surface area, structure defect, and crystalline size.[28] In this work, the samples prepared at various temperature for 48 h have the similar phase structure and band gap. BET surface area of the synthesized samples tends to decrease slightly with an increase in the hydrothermal temperature (S1) which does not lead to the difference among samples. There are other two conflicting factors that affect the overall photocatalytic activity in an opposite way (i.e., the number of defects and the surface area).[29] Hence, defects in the crystal structure are considered as the main factor influencing the photocatalytic activity in the present system. In general, lattice defects may act as recombination centers for photoinduced electrons and holes, reducing the total photocatalytic activity significantly. Many lattice defects in the form of hydroxyl groups and cation vacancies exist in the samples prepared by hydrothermal synthesis, and their

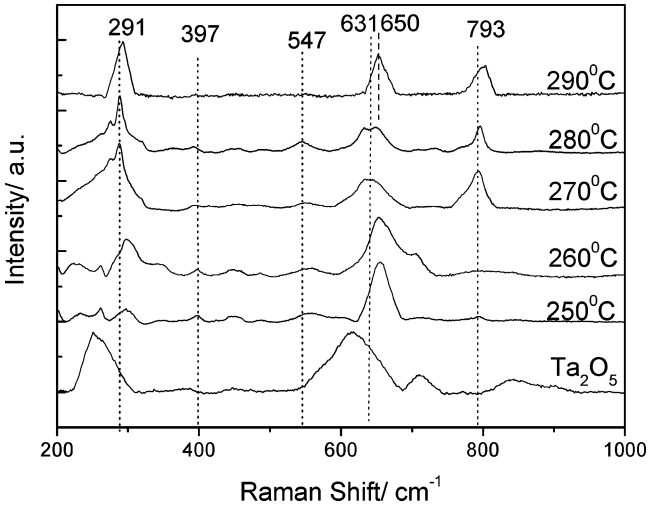

Figure 8. Raman spectroscopy of $BaTa_2O_6$ samples prepared at various reaction temperatures (250−290 °C) for 48 h.

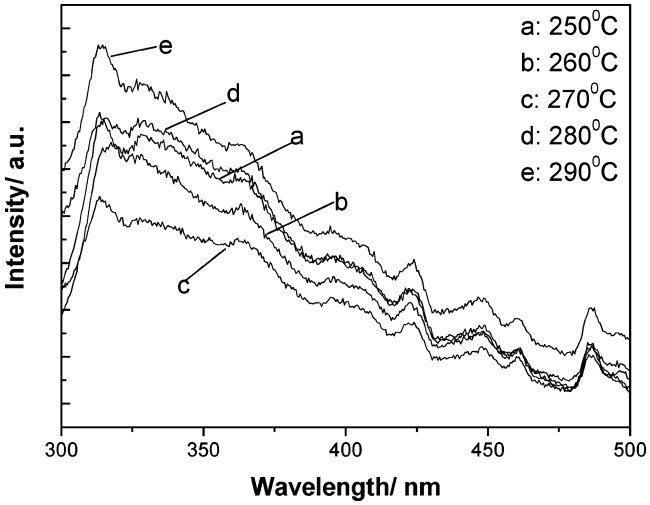

Figure 9. PL spectra recorded in $BaTa_2O_6$ nanorods obtained at various temperatures for 48 h.

concentration increased with decreasing particle size.[30] Several studies suggest that chemically bound hydroxyl (OH^-) groups are incorporated directly into the lattice, presumably on oxygen sites. The rapid increase in the photocatalytic activity with increasing temperature when going from 250 °C to 270 °C comes from the increase of crystalline and the decrease of lattice defects. The photocatalytic activities for higher temperature samples (280 °C, 290 °C) may be attributed to the increased defects in the structure though with a high crystallinity. It will be discussed in the next sections. The highest activity of the $BaTa_2O_6$ sample (270 °C) may result from the least defects in crystallinity.

Raman, FT-IR, and PL analyses of the samples are performed to examine the defects in $BaTa_2O_6$ nanorods. Raman spectra of $BaTa_2O_6$ samples obtained at different temperatures are shown in Figure 8. The broad peak at 793 cm^{-1} corresponds to A_{1g} (O) modes and is assigned to stretching vibrations of short Ta−O bonds in TaO_6 octahedron which stick out into the interlayer spaces.[31] This peak cannot be observed in samples prepared at 250 °C and 260 °C due to the poor crystalline. The peak at 547 cm^{-1} results from A_{1g} (Ta) modes and the bands at about 397 and 430 cm^{-1} are associated with internal vibrations of oxygen octahedra, A_{1g} (O) and 2Eg(O) Raman phonon modes, respectively. The main band in $BaTa_2O_6$ at 630−650 cm^{-1} can be attributed to the Ta−O stretching mode of Ta−O−Ta chains. This band is mainly due to a totally symmetric combination of coupled Ta−O stretching modes in the chains of tantalum octahedral. In the Ta_2O_5 sample, the major band at 621 cm^{-1} is the characteristic band which comes from the TaO_6 octahedra-sharing corner structure.[32] However, this characteristic band shifts to high frequency at 650 cm^{-1} in $BaTa_2O_6$, indicating a break of the corner-sharing structure of Ta−O polyhedra in Ta_2O_5 crystalline form and the formation of $BaTa_2O_6$. As is shown in Figure 8, Raman shifts to the higher frequencies of the samples are different. The spectra of $BaTa_2O_6$ (250 °C, 260 °C, 290 °C) show a band that is shifted by up to 30 cm^{-1} (only up to 10 cm^{-1} as for 270 °C). The changes about this band are associated with the defects in $BaTa_2O_6$ samples. According to the results of reference 33, we think the position of this Raman band reflects the change of defects in $BaTa_2O_6$ samples. The larger the up-shifts for this band, the more defects in the crystal structure. The bands at 291 cm^{-1} arise from the breathing vibration of the long Ta−O bonds and Ta−O−Ta (bridging O atom) T_{2g} bending mode.[34] With the increase of hydrothermal temperature, the bands at 251 cm^{-1} and 625 cm^{-1} vanish and two new peaks at 290 cm^{-1} and 650 cm^{-1} appear. It can be seen that the full widths at half-maximum of 631 cm^{-1} and 291 cm^{-1} for samples (270 °C, 280 °C) are larger than that of others, and Raman peaks also shift to lower position. On the basis of the above results, it can be concluded that less defects exist in $BaTa_2O_6$ nanorods (270 °C, 280 °C), resulting in higher photocatalytic activity than other samples.

Figure 9 shows the photoluminescence spectra of $BaTa_2O_6$ nanorod samples synthesized at various hydrothermal temperatures for 48 h. All the samples exhibit obvious PL signals with a similar curve shape. Four emission bands, including two violet emissions at around 300−350 nm and 360−380 nm, a blue band at about 420−470 nm, and a green band at about 480 nm, are observed. This is considerably different from that observed in typical bulk $BaTa_2O_6$crystals, which usually exhibit a broad blue peak at 420 nm.[8c] The main emission peak at about 315 nm is equivalent to 3.94 eV and is consistent with their onset of DRS (S2). The violet emission of $BaTa_2O_6$ nanorods can be ascribed to the radiative defects related to the interface traps existing at the grain boundaries and the electron transition from the bottom of the conduction band to the top of the valence band.[35] The blue-band emission may originate from the recombination of oxygen vacancies with oxygen interstitials or other defects.[36] Considering the wavelength of PL signals and the DRS results, it can be confirmed that these PL signals mainly result from the defects.[37] With the improvement of crystallinity in samples, the intensity of PL emission theoretically drops to zero atoom temperature. As for the samples obtained by the hydrothermal method, the high intensity of the luminescence could be due to the defects in the structure.[38] PL emission spectra discloses the efficiency of charge carrier trapping, immigration, transfer, and the fate of electrons and holes in the semiconductor. The variation of PL intensity may result from the change of defect state on the surface. The difference of PL spectra in Figure 9 results from the different density of structure defects in samples formed in various reaction temperatures. The obvious lower intensity of PL at 315 nm can be ascribed to the lower recombination rate of photogenerated electrons and holes under UV irradiation. It reasonably leads to the higher photocatalytic activity of the sample since the photodegradation reactions are evoked by these charge carriers.[39] The intensity of PL greatly decreased with the increase of reaction temperature from 250 °C to 290 °C, and the lowest intensity of PL was observed in the $BaTa_2O_6$ nanorod sample (270 °C), indicating that less defects exist in the structure. As the temperature increases, the

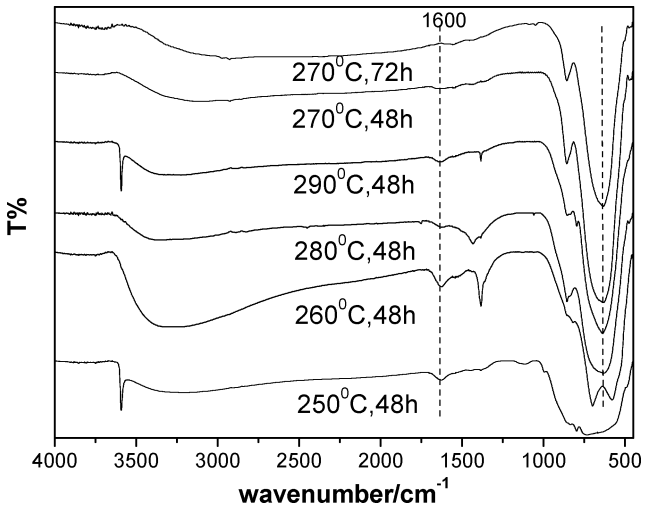

Figure 10. FT-IR spectra of $BaTa_2O_6$ nanorod samples obtained at various temperatures.

decrease in the photocatalytic activity may be interpreted as the increase of defects in crystals formed in the dissolution−recrystallization process.

As a consequence of the disruption of Ta−O−Ta chains and partial leaching of Ta atom, the formation of new hydroxyl groups is observed in FT−IR spectra from $BaTa_2O_6$ nanorods. FT−IR spectra of $BaTa_2O_6$ samples obtained at various temperatures are shown in Figure 10. $BaTa_2O_6$ nanorod samples show the main bands at 500−750 cm^{-1}, which are attributed to Ta−O stretching and Ta−O−Ta bridging stretching modes. No change of the absorption peak at about 630 cm^{-1} can be found as the $BaTa_2O_6$ phase formed at 270 °C. The peak of 1620 cm^{-1} and the broadband at 3300−3600 cm^{-1} are assigned to the bending vibration of O−H and O−H vibration of H_2O. The sharp absorption peaks around 3600 cm^{-1} for 250 °C and 290 °C are characteristic of free hydroxyl group stretches in the framework lattice.[40] OH^- stretching vibration is sensitive to the change of the environment around the ion; therefore, OH-absorption spectra can be used as a probe for defects. The intensities of OH^-vibration bands decrease and the intensities of Ta−O vibration bands increase with hydrothermal temperature. Impurities almost completely disappear in the samples prepared at 270 °C. It has been shown that the removal of impurity groups promotes the rearrangement of the Ta−O network and the crystallization of $BaTa_2O_6$ at 270 °C. But when the temperature is over 270 °C, OH^- peaks also appear (see Figure 10). At 290 °C, two peaks at about 3600 cm^{-1} and 1620 cm^{-1} exist, which correspond to the hydroxyl group in $BaTa_2O_6$ nanorods, indicating that the number of hydrogen-related defects increases. It is very important to restrain the recombination of photoinduced electrons and holes for high photocatalytic activity. Defects in photocatalysts are always recombination centers of photoinduced electrons and holes, which will result in the decrease of photocatalytic activity. The effectiveness of the photocatalytic reaction was strongly dependent on the defects. On the basis of the above results, it can be concluded that the defect number in the sample prepared at 270 °C is the least, compared with other samples at various temperatures. Therefore, the nanorod sample prepared at 270 °C shows the best activity.

On the basis of the above results, defects are found in $BaTa_2O_6$ nanorods prepared by the hydrothermal method and the number of the hydrogen-related defects varies with the hydrothermal temperature. The photocatalytic activity is greatly governed by the defects, and the photocatalytic activity decreases with an increase in the defects.

4. Conclusion

Hexagonal $BaTa_2O_6$ with controllable morphology can be synthesized by means of a relatively simple hydrothermal reaction. The growth mechanism of the nanorods obeys a dissolution−crystallization process. The photocatalytic activity of $BaTa_2O_6$ nanorods was mainly governed by the number of hydrogen-related defects formed during hydrothermal processes. High photocatalytic activity of the nanocrystalline photocatalyst can be obtained by reducing the hydrogen-related defects via control of the reaction conditions.

Acknowledgment. This work was partly supported by Chinese National Science Foundation (20433010, 20571047).

Supporting Information Available: Specific surface area (BET) and UV−vis diffraction spectra (UV−DRS) of $BaTa_2O_6$ nanorod samples for different hydrothermal temperatures. This material is available free of charge via the Internet at http://pubs.acs.org.

References and Notes

(1) (a) Fujishima, A.; Honda, K. *Nature* **1972**, *37*, 238. (b) Machida, M.; Yabunaka, J.; Kijima, T. *Chem. Commun.* **1999**, 1939.
(2) (a) Turchi, G. S.; Ollis, D. F. *J. Catal.* **1990**, *122*, 178. (b) Abe, R.; Shinohara, K.; Tanaka, A.; Hara, M.; Kondo, J.; Domen, K. *Chem. Mater.* **1997**, *9*, 2179.
(3) (a) Hoffmann, M. R.; Martin, S. T.; Choi, W. Y.; Bahnemann, D. W. *Chem. Rev.* **1995**, *95*, 69. (b) Hwang, S.-J.; Petucci, C.; Raftery, D. *J. Am. Chem. Soc.* **1997**, *119*, 7877.
(4) (a) Inoue, Y.; Kubokawa, T.; Sato, K. *J. Phys. Chem.* **1991**, *95*, 4059. (b) Anderson, C.; Bard, A. J. *J. Phys. Chem. B* **1997**, *101*, 2611.
(5) Vinodgopal, K.; Kamat, P. V. *Environ. Sci. Technol.* **1995**, *29*, 841.
(6) Takata, T.; Furumi, Y.; Shinohara, K.; Tanaka, A.; Hara, M.; Kondo, J. N.; Domen, K. *Chem. Mater.* **1997**, *9*, 1063.
(7) Kudo, A.; Kato, H.; Nakagawa, S. *J. Phys. Chem. B* **2000**, *104*, 571.
(8) (a) Zou, Z.; Ye, J.; Arakawa, H. *J. Phys. Chem. B* **2002**, *106*, 13098. (b) Zou, Z.; Ye, J.; Sayama, K.; Arakawa, H. *Nature* **2001**, *414*, 625.
(9) (a) Kato, H.; Kudo, A. *Chem. Lett.* **1999**, 1207. (b) Kato, H.; Kudo, A. *Chem. Phys. Lett.* **1998**, *295*, 487. (c) Kato, H.; Kudo, A. *Catal. Today* **2003**, *78*, 561. (d) Kudo, A.; Kato, H.; Tsuji, I. *Chem. Lett.* **2004**, 1504.
(10) Yoshioka, K.; Petrykin, V.; Kakihana, M.; Kato, H.; Kudo, A. *J. Catal.* **2005**, *231*, 102.
(11) Bonanni, M.; Spanhel, L.; Lerch, M.; Fuglein, E.; Muller, G.; Jermann, F. *Chem. Mater.* **1998**, *10*, 304.
(12) Maira, A. J.; Yeung, K. L.; Lee, C. Y.; Yue, P.; Chan, C. *J. Catal.* **2000**, *192*, 185.
(13) Zhang, C.; Zhu, Y. *Chem. Mater.* **2005**, *17*, 3537.
(14) Mao, Y.; Wong, S. S. *J. Am. Chem. Soc.* **2006**, *128*, 8217.
(15) Urban, J. J.; Yun, W. S.; Gu, Q.; Park, H. *J. Am. Chem. Soc.* **2002**, *124*, 1186.
(16) Kasuga, T.; Hiramatsu, M.; Hoson, A.; Sekino, T.; Niihara, K. *Adv. Mater.* **1999**, *11*, 1307.
(17) Tian, Z.; Voigt, J. A.; Liu, J.; Mckenzie, B.; Xu, H. *J. Am. Chem. Soc.* **2003**, *125*, 12384.
(18) Gao, X.; Bao, J.; Pan, G.; Zhu, H.; Wu, F.; Song, D. *J. Phys. Chem. B* **2004**, *108*, 5547.
(19) Setter, N. *J. Eur. Ceram. Soc.* **2001**, *21*, 1279.
(20) Galasso, F.; Layden, G. K.; Ganung, G. *Mater. Res. Bull.* **1968**, *3*, 397.
(21) Joshi, U. A.; Lee, J. S. *Small* **2005**, *1*, 1172.
(22) Miao, L.; Tanemura, S.; Toh, S.; Kaneko, K.; Tanemura, M. *J. Cryst. Growth* **2004**, *264*, 246.
(23) Yu, S.; Biao, L.; Mo, M.; Huang, J.; Liu, X.; Qian, Y. *Adv. Funct. Mater.* **2003**, *13*, 639.
(24) Quere, D.; Di Meglio, J.-M.; Brochard-Wyart, F. *Science* **1990**, *249*, 1256.
(25) (a) Peng, Z.; Peng, X. *J. Am. Chem. Soc.* **2002**, *124*, 3343. (b) Peng, X.; Manna, L.; Yang, W.; Wickham, J.; Scher, E.; Kadavanich, A.; Alivisatos, A. P. *Nature* **2000**, *404*, 59.
(26) Chen, C.; Zhao, W.; Lei, P.; Zhao, J.; Serpone, N. *Chem. Eur. J.* **2004**, *10*, 1956.
(27) (a) Park, H.; Choi, W. *J. Phys. Chem. B* **2003**, *107*, 3885. (b) Kim, H.G.; Borse, P. H.; Choi, W.; Lee, J. S.*Angew. Chem., Int. Ed.* **2005**, *44*, 4585.
(28) Kim, S. H.; Choi, W. Y. *J. Phys. Chem. B* **2005**, *109*, 5143.
(29) Yamashita, Y.; Yoshida, K. *Chem. Mater.* **1999**, *11*, 61.
(30) Chen, H.; Chen, Y. *Ind. Eng. Chem. Res.* **2003**, *42*, 473.

(31) (a) Kudo, A.; Sakata, T. *J. Phys. Chem.* **1996**, *100*, 17323. (b) Kudo, A.; Kondo, T. *Mater. Chem.* **1997**, *7*, 777.

(32) Chen, Y.; Fierro, J. L. G.; Tanaka, T.; Wachs. I. E. *J. Phys. Chem. B* **2003**, *107*, 5243.

(33) Llabrési Xamena, F. X.; Damin, A.; Bordiga, S.; Zecchina, A. *Chem. Commun.* **2003**, 1514.

(34) Surendran, K. P.; Sebastian, M. T.; Mohanan, P.; Moreira, R. L.; Dias, A. *Chem. Mater*. **2005**, *17*, 142.

(35) Mahamuni, S.; Borgohain, K.; Bendre, B. S.; Leppert, V. J.; Risbud, S. H. *J. Appl. Phys.* **1999**, *85*, 2861.

(36) Bouquet, V.; Vasconcelos, N. S. L. S.; Aguiar, R.; Pinheiro, C. D.; Leite, E. R.; Pizzani, P. S.; Varela, J. A.; Longo, E.; Boschi, T. M.; Lanciotti, F.; Machado, M. A. C. *Ferroelectrics* **2003**, *288*, 315.

(37) Jing, L.; Xin, B.; Yuan, F.; Xue, L.; Wang, B.; Fu. H. *J. Phys. Chem. B* **2006**, *110*, 17860.

(38) Wang, Q.; Zhang, D.; Xue, Z.; Hao, X. *Appl. Surf. Sci.* **2002**, *201*, 123.

(39) Yu, J.; Yu, J.; Ho, W. K.; Zhang, L. *Chem. Mater*. **2002**, *14*, 3808.

(40) Li, Z.; Yu, T.; Zou, Z.; Ye, J. *Appl. Phys. Lett.* **2006**, *88*, 071917.